

# Understanding the PSCz Galaxy Power Spectrum with N-body Simulations

Mark C. Neyrinck, Andrew J. S. Hamilton

*JILA, APS Dept, University of Colorado, Boulder, CO 80309;*  
Mark.Neyrinck@colorado.edu; Andrew.Hamilton@colorado.edu

Nickolay Y. Gnedin

*Center for Astrophysics and Space Astronomy, APS Dept, University of Colorado, Boulder,*  
*CO 80309; gnedin@casa.colorado.edu*

## ABSTRACT

By comparing the PSCz galaxy power spectrum with the results of nested pure dark matter N-body simulations, we try to understand how infrared-selected galaxies populate dark-matter haloes, paying special attention to the method of halo identification in the simulations. We thus test the hypothesis that baryonic physics negligibly affects the distribution of galaxies down to the smallest scales yet observed. We are successful in reproducing the PSCz power spectrum on scales  $\lesssim 40 h \text{ Mpc}^{-1}$ , near our resolution limit, by imposing a central density cutoff on simulated haloes, which gives a rough minimum mass of haloes in which PSCz galaxies formed.

## 1. Introduction

The large-scale structure of the universe can be difficult to study when only the tips of icebergs can be observed. We can catalogue the positions and redshifts of galaxies, and can obtain glimpses of the intergalactic environment by observing the Lyman-alpha forest, but the dark matter, the component which plays the largest role in our current paradigm of structure formation, remains obscure. In this paper, we try to connect underlying dark matter icebergs (haloes) to the tips (galaxies) we can see.

Only in the last few years have we claimed to have a successful cosmological model, the “concordance”  $\Lambda$ CDM model. Its loose ends do seem tieable, but some areas remain largely mysterious: for example, the formation of galaxies within dark matter haloes, and the resulting relationship between them at the present epoch. Here, we investigate this

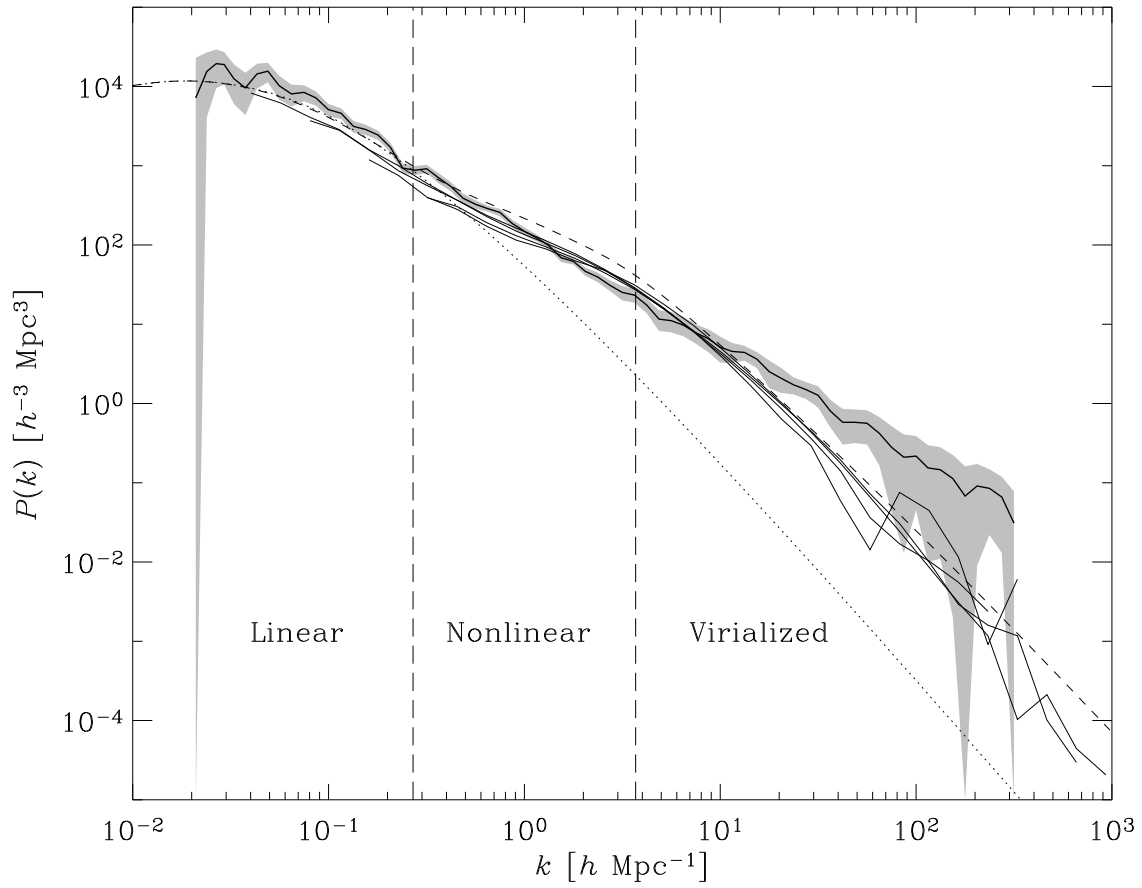


Fig. 1.— Comparison of the dark matter power spectra from the simulations (thin solid curves) to the linear power spectrum (dotted curve) and the nonlinear power spectrum (dashed curve) evolved from the linear power spectrum using the method of Peacock & Dodds (1996). The PSCz power spectrum also appears, surrounded by a grey band.

relationship through their distributions, most succinctly quantified by the power spectrum, or its Fourier dual, the correlation function. Currently, the most extensive measurement of a power spectrum of observed galaxies, ranging over 4.5 decades of wavenumber, is by Hamilton & Tegmark (2002, hereafter HT). It was made from the PSCz (Point Source Catalogue Redshift) catalogue (Saunders et al, 2000) of galaxies observed with the IRAS infrared satellite. There will soon be a flood of galaxy clustering data, for example from the Sloan Digital Sky Survey (York et al 2000) and the Two-Degree Field (Lewis et al 2002) survey. Early data (e.g. Zehavi et al 2002, Percival et al 2001) suggest that clustering properties vary with galaxy morphology, luminosity, and color. Here we restrict ourselves to PSCz infrared galaxies, but with excellent optical data differentiated by color, an approach such as ours will soon be able to say more about the types of galaxies which inhabit different sorts of dark matter haloes.

As with other past measurements of galaxy power spectra, for example from the APM galaxy survey (Baugh 1996), HT found a roughly power law form. This is not produced from pure dark matter in the current concordance  $\Lambda$ CDM cosmological model. Fig. 1 shows the PSCz power spectrum along with linear and nonlinear power spectra for the concordance  $\Lambda$ CDM model, and also dark matter power spectra from our simulations. The nonlinear dark-matter spectrum traces the linear spectrum at large scales, but at smaller, nonlinear scales, it rises above it because waves on the scale of collapsing structures grow faster than in the waves in the linear regime. At even smaller scales, virialization slows growth, producing a downward inflection. Fig. 2 shows the bias factors between PSCz galaxies, as well as our best-fit haloes, and the dark matter in our simulations.

Numerous attempts have been made to understand scale-dependent bias. The halo model of large-scale structure (reviewed by Cooray & Sheth, 2002) assumes the existence of small, bound objects (haloes) which are clustered according to the linear power spectrum. Galaxy clustering statistics such as the correlation function can then be calculated as the sum of two terms describing pairs of galaxies from the same and from different haloes. This can make use of a Halo Occupation Distribution, HOD (Benson 2001; White, Hernquist, & Springel 2001; Berlind & Weinberg 2002, Berlind et al 2002), which describes the number of galaxies which inhabit a halo of a given mass. In this context, a halo is defined as a region at least 200 (typical of virialization) times more dense than the background. The approximations of the halo model permit analytic models for the bias between galaxies and dark matter (e.g. Seljak 2000, Sheth & Jain 2002), which can be quite useful. However, no one would claim that the universe is just a set of spherical haloes. The halo model ignores structures such as sheets and filaments which are found in N-body simulations, and only considers halo substructure in a statistical fashion.

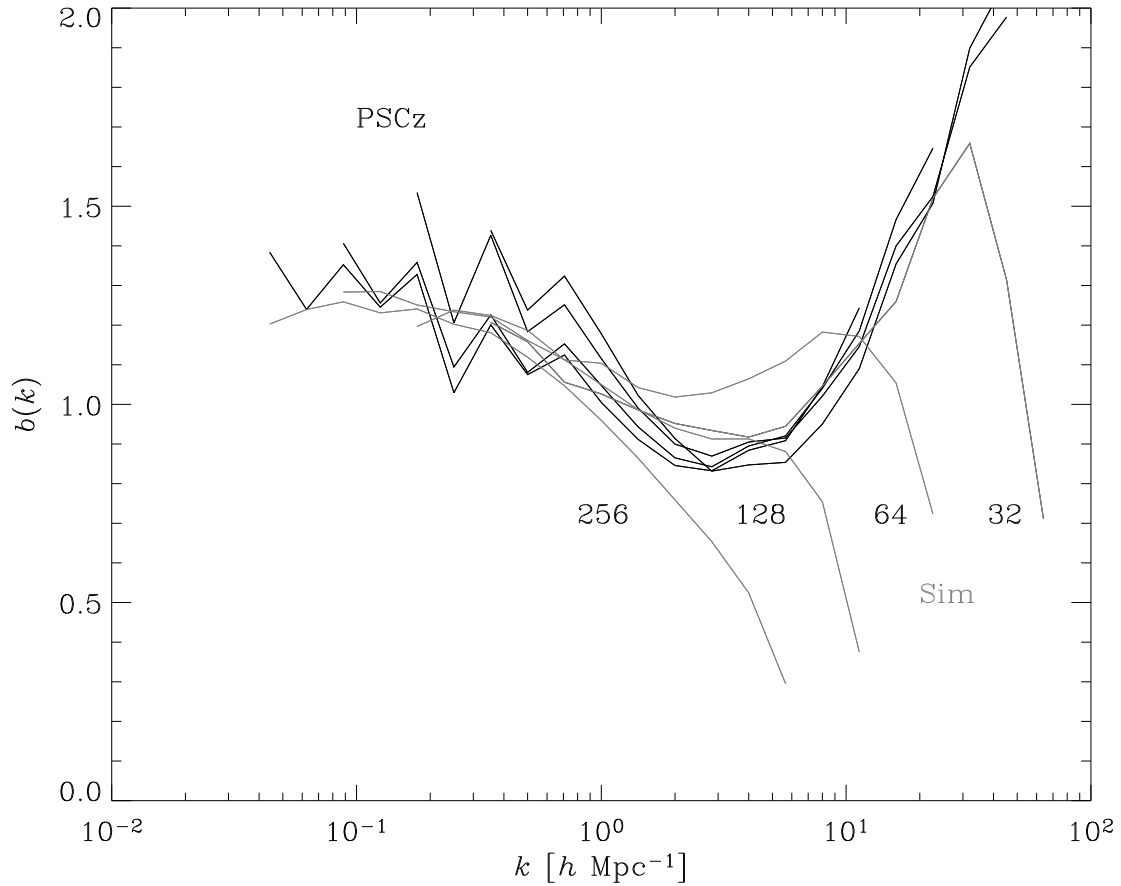


Fig. 2.— Bias factors for the PSCz power spectrum (black) and the simulated sets of haloes (grey). The PSCz bias curves are  $b_{\text{PSCz}}(k) = \sqrt{P_{\text{PSCz}}(k)/P_{\text{dm}}(k)}$ , with a different  $P_{\text{dm}}$  for each simulation. The simulation bias curves are  $b_{\text{sim}}(k) = \sqrt{P_{\text{haloes}}(k)/P_{\text{dm}}(k)}$ , again running through the simulations.

Semi-analytic galaxy formation models (e.g. White & Frenk 1991, Kauffmann et al 1999, Benson et al 2000, Somerville et al 2001, Mathis et al 2002) and hydrodynamic simulations (e.g. Katz, Hernquist, & Weinberg 1992, Cen & Ostriker 2000, Davé et al 2000, Pearce et al 2001, White, Hernquist, & Springel 2001, Yoshikawa et al 2001), have also been successfully applied to the problem of bias. While these approaches directly give the relationship between galaxies and dark matter, some of the galaxy formation prescriptions in semi-analytic models can be rather ad hoc, and it is not clear that hydrodynamic simulations correctly treat every piece of relevant baryonic physics.

In this paper, we take a somewhat different tack: we directly fit the PSCz power spectrum to dark matter-only N-body simulations. We are thus seeing how far we can take the assumption that on intergalactic scales, baryonic physics negligibly affects the clustering of haloes which contain observed galaxies. A similar study, without fitting to specific observations, has been undertaken by Kravtsov & Klypin (1999).

We also do not employ a HOD framework. Such a statistical placement of galaxies in haloes is useful in constructing an analytic model or when faced with poor resolution, and can aid intuition. Our approach is more direct: if a halo is defined not as a region above a certain overdensity, but as a region gravitationally bound to a significant (an admittedly vague adjective) maximum in the density field, a definition which would admit subhaloes without their parent haloes, then the number of galaxies detected by a redshift survey inside a halo is either zero or one.

We pay particular attention to the halo-finding algorithm we use to go from a dark matter distribution to a distribution of haloes. This is the most nontrivial step in comparing the results of simulations to the observed galaxy power spectrum. We want to understand the effects of resolution on the halo-finding algorithm; this is one reason that we ran four simulations of varying mass resolution.

## 2. Method

### 2.1. The Simulations

The PSCz power spectrum spans 4.5 decades of wavenumber; to replicate this dynamic range in an N-body simulation would be unfeasible. For this reason, and also to test for resolution effects, we ran four manageably-sized  $256^3$ -particle simulations, of comoving box size 32, 64, 128, and 256  $h^{-1}$  Mpc, with an adaptive P<sup>3</sup>M code (Bertschinger 1991). A simulation of box size less than about 32  $h^{-1}$  Mpc would miss significant tidal forces from large-scale fluctuations, and also could not form large clusters that appear with low number

densities in nature. The values of cosmological parameters we used in the simulation were from the concordance model of Wang, Tegmark, and Zaldarriaga (2002):  $\Omega_m = 0.34$ ,  $\Omega_\Lambda = 0.66$ ,  $h = 0.64$ , and  $n = 0.93$ . We calculated the transfer function of the initial conditions with the code of Eisenstein & Hu (1999), which returned a value of  $\sigma_8 = 0.63$ , the rms fluctuation of mass in spheres of radius  $8 h^{-1}$  Mpc.

There were two resolution issues to consider: mass resolution and spatial resolution. The mass resolution, i.e. the mass of a particle in the simulation, depends on the number of particles per unit volume. So, the mass resolution in the four simulations necessarily changes with box size. However, we decided to use the same spatial resolution (softening length) for all simulations:  $10 h^{-1}$  kpc, roughly the lowest scale probed in the PSCz power spectrum.

Unlike many cosmological simulations, our softening length was fixed in physical, not comoving (Eulerian, not Lagrangian), coordinates. This means that at early epochs, the comoving softening length was larger, at maximum about 1/6 the mean interparticle separation in the  $32 h^{-1}$  Mpc simulation, and less by factors of two in the others. The first haloes to collapse at  $z \approx 10$  turn out to be quite important in determining the fine structure of haloes at  $z = 0$ . The first haloes contain only a few particles at  $z \approx 10$ , and a small comoving smoothing length can make their relaxation times tiny, resulting in an overproduction of small, relaxed structures (Moore 2001; Binney and Knebe 2002). By having a fairly large comoving softening length at early times, we hope to have mitigated this problem.

We wanted the four simulated regions to be as similar as possible under the constraints of periodic boundary conditions, enabling us to compare structures in the four simulations to each other. Bertschinger (2001), building on the work of Pen (1997), developed a simple formalism to generate Gaussian random fields with multiple levels of resolution, which we used to nest the initial conditions. Effectively, this means that the phases of fluctuations matched in the centers of each set of initial conditions. An animation depicting the nesting of the boxes can be found at <http://casa.colorado.edu/~neyrinck/nesthalf.mpg>. The zone of agreement between two simulations of box size  $b$  and  $b/2$  is a central cube of side length roughly  $b/4$ ; a greater zone of agreement is not possible since the smaller box has to obey periodic boundary conditions.

We also selected our initial conditions so that the central region common to the four simulations would have a structure similar to the Local Group and its environs. In this way, we hoped to replicate some features of the way the PSCz observations were made, looking out from the Milky Way, in a slightly overdense region on the outskirts of a modest-sized supercluster. The highest-resolution information in the simulations is from the smallest box, just as the galaxies closest to each other in the PSCz catalogue came from regions close to the Milky Way.

To obtain these special initial conditions, we generated ten sets of initial conditions for a  $256 h^{-1}$  Mpc simulation on a  $256^3$  mesh, and ran them to the present epoch using a (fast but low-resolution) PM code. We counted particles in each cell of side length  $8 h^{-1}$  Mpc, the traditional scale of nonlinearity, over which we can trust the results of the quick PM code. This gave a  $32^3$  grid of dark matter density estimates  $\rho$  at the present epoch from each set of initial conditions. The same was done for the PSCz catalogue, binning galaxies on a  $4^3$  grid of  $8 h^{-1}$  Mpc cells with the Milky Way at the center. This resulted in a galaxy number density ( $n_{\text{PSCz}}$ ) grid of total side length  $32 h^{-1}$  Mpc, far enough to enclose the local supercluster. We then compared all cubes 4 cells on a side from the simulations to the galaxy density grid. The comparison was made by minimizing the sum of  $(\rho - n_{\text{PSCz}})^2$  over nine  $16 h^{-1}$  Mpc cubes: eight from dividing the  $32 h^{-1}$  Mpc cube into octants, and one more in the center. We then shifted the best-fit region to the center of the  $256 h^{-1}$  Mpc set of initial conditions before calculating the lower-box size initial conditions. Table 1 shows these densities for the best fit. Unfortunately, this procedure did not result in structures with obvious visible similarity to the local group, but the statistical similarity is reassuring.

Although similar, the inner regions of the four simulations were not identical after evolving them to the present epoch. Large-scale power caused bulk motion in the central region, moving it away and distorting it slightly from its original position. To assess this effect, we approximated it to first order with the sum of a translation and a linear transformation, an asymmetric tensor which in general could include shear and rotation:

$$r_i^{(2)} = C_{ij} r_j^{(1)} + s_i, \quad (1)$$

where  $r_i^{(m)}$  is the  $i$ th coordinate in the central region of simulation  $m$ ,  $C_{ij}$  is a deformation tensor, and  $s_i$  is a translation vector.

Figure 3 shows particles initially in the central  $16 h^{-1}$  Mpc box from all simulations in the present epoch. The region from the  $32 h^{-1}$  Mpc simulation is untransformed, with the other three regions translated and deformed to fit best onto it. To calculate the shift

Table 1: Choice of initial conditions. Both the PSCz galaxy density and the ‘‘Simulation’’ dark matter density are normalized to one.

	PSCz	Simulation	PSCz	Simulation
Corner boxes	1.49255	1.11328	0.83325	0.50146
	0.49410	0.76367	0.31982	0.47900
	1.45612	1.20386	2.35201	1.99805
	1.60033	1.63550	0.39196	0.83447
Central box	1.36050	1.10596		

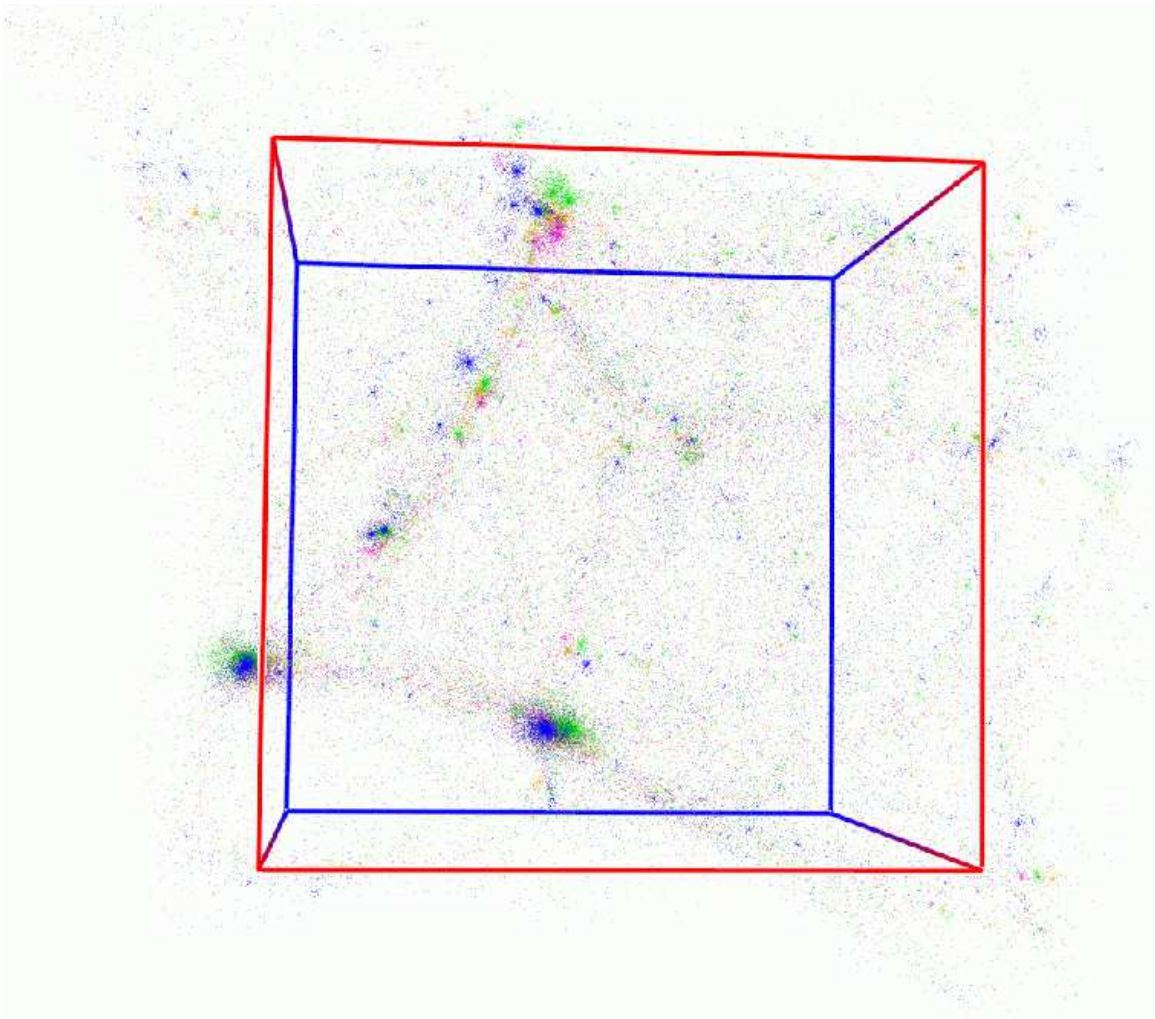


Fig. 3.— The region originally in the central  $16 h^{-1}$  Mpc region of each simulation. Particles from the  $32$ ,  $64$ ,  $128$ , and  $256 h^{-1}$  Mpc simulations appear in magenta, orange, green, and blue, respectively. The sets of particles from simulations of boxsize greater than  $32 h^{-1}$  Mpc have undergone a translation and linear transformation to lie on the set from the (untransformed)  $32 h^{-1}$  Mpc simulation. All particles from the central region are shown for the  $128 h^{-1}$  Mpc simulation, and the number densities of particles from other simulations are adjusted by factors of eight to match. Thus,  $1/8$  and  $1/64$  of the particles from the  $64$  and  $32 h^{-1}$  Mpc simulations appear. In the  $256 h^{-1}$  Mpc case, the number density was octupled by adding new particles which bisect lines joining particles adjacent on the initial mesh. The figure was produced using Nick Gnedin’s IFRIT visualization tool, at <http://casa.colorado.edu/~gnedin/IFRIT/>.

and deformation, we compared the present-epoch positions of particles which had occupied the same place in the initial conditions; i.e. with the same Lagrangian positions. Since mass resolution changes across simulations, it was necessary to average together positions of particles (in sets of  $2^3$ ,  $4^3$ , or  $8^3$ ) to compare positions in a smaller box size simulation to those in a larger one.

We calculated the translation vector  $s_i$  with  $\langle r_i^{(2)} - r_i^{(1)} \rangle$ , where the angular brackets denote an average over particles. As for the deformation tensor  $C_{ij}$ , consider the quantity  $\langle (r_i^{(2)} - s_i)r_k^{(1)} \rangle$ . Assuming that Eqn. (1) holds, this equals  $C_{ij}\langle r_j^{(1)}r_k^{(1)} \rangle$ . Thus, where  $B_{ik} = \langle (r_i^{(2)} - s_i)r_k^{(1)} \rangle$  and  $A_{jk} = \langle r_j^{(1)}r_k^{(1)} \rangle$ ,

$$C_{ij} = B_{ik}(A^{-1})_{kj}. \quad (2)$$

The translation vectors  $s_i$  from the 64, 128, and 256  $h^{-1}$  Mpc simulations to the 32 had magnitudes 2.78, 4.43, and 5.92  $h^{-1}$  Mpc, respectively. The deformation tensors  $C_{ij}$  were close to identity matrices, as one would hope; the diagonal elements were all between 0.89 and 1.06 except for one outlier at 0.81, and the off-diagonal elements had magnitudes below (mostly well below) 0.06. With the first-order adjustment, the agreement is still not perfect, but we expect the shear from large-scale waves outside the inner box to change slightly over its length; moreover, slight differences are likely to amplify when nonlinearly evolved.

## 2.2. Halo finding

To compare to the observed galaxy power spectrum, it is necessary first to find haloes in the set of dark matter particles returned by the simulations. Although they do reasonable jobs, no halo-finding algorithm (HFA) is perfect. In some analyses of N-body simulations, surprisingly little discussion is given of the choice of HFA.

The first step of most HFAs is to estimate the density, a quantity which is not obviously defined given only a set of particles. DENMAX (Bertschinger & Gelb 1991) uses an Eulerian approach, calculating the density on a fine mesh by smoothing each particle with a Gaussian of a fixed size, called the smoothing length,  $r_{\text{smoo}}$ . The mesh size,  $r_{\text{smoo}}/3$ , is chosen so that a Gaussian is well-resolved. A Lagrangian approach (HOP, Eisenstein & Hut 1998) uses a fixed number  $N_{\text{dens}}$  of nearest-neighbor particles to estimate the density at the position of each particle, and also uses a few other parameters. DENMAX has a fixed spatial resolution, while HOP effectively has a fixed mass resolution. The results of both methods are strongly dependent on their free parameters,  $r_{\text{smoo}}$  or  $N_{\text{dens}}$ .

Although DENMAX takes much more time to run than HOP, we ended up using a

variant of DENMAX. We found that DENMAX is capable of finding smaller haloes than HOP, down to about ten particles. DENMAX works by moving particles along density gradients until they are at a maximum. It then uses a “Friends-of-Friends” algorithm, finding clusters of moved particles closer than a small linking length (1/1024 times the box size) to each other. The last step is to “unbind” iteratively any particles whose energies exceed the escape energy from their haloes. The output of DENMAX is a list of haloes with their masses (number of bound particles), and their position and velocity centroids.

In DENMAX, a large smoothing length smears out close pairs of haloes, while a small smoothing length, with its higher density threshold, fails to include the outskirts of haloes in their mass, and also misses isolated, less-dense haloes. Gelb & Bertschinger (1994) discuss some effects of DENMAX resolution. Empirical tests have indicated that setting  $r_{\text{smoo}} = 1/5$ , in units of the mean interparticle separation, yields a halo mass spectrum similar to that given by the Press-Schechter (1974) formalism, a useful, though not omniscient, guide. This choice of  $r_{\text{smoo}}$  makes some sense theoretically, too, since the spherical collapse model (Gunn & Gott 1972) predicts that a virialized object is  $\delta \approx 180$  times denser than the background in a standard flat ( $\Omega_m = 1$ ) cosmology, and somewhat higher than that in a  $\Lambda$ CDM cosmology. Fiducially, regions of overdensity 200 and above are virialized, corresponding to a smoothing length of  $1/200^{1/3}$ , about 1/5.

We applied DENMAX with the canonical smoothing length to the results of each simulation, and calculated halo power spectra. The halo-finding resolution we obtained was rather poor; there was a small-scale downturn in each power spectrum starting at significantly larger scales than the simulation’s softening length. We therefore tried halving the DENMAX smoothing length to  $r_{\text{smoo}} = 1/10$ , and succeeded in extending the power law in the correlation function to smaller scales by about a factor of two. The smaller smoothing length evidently picked out subhaloes which the canonical smoothing length had merged together. A small smoothing length is desirable in detecting subhaloes within a halo, since in a halo, the spatial scales involved are smaller, and the background density is higher.

We wanted to use higher resolution in higher-density regions without forsaking the advantages of the canonical  $r_{\text{smoo}}$  in lower-density regions. We therefore used an algorithm which we call DENMAX<sup>2</sup>, in which DENMAX is run as normal with the canonical  $r_{\text{smoo}} = 1/5$ , but then is applied to each returned halo separately with  $r_{\text{smoo}} = 1/10$ . Fig. 4 shows the effect of this extra substructure on the best-fit (defined below) halo correlation functions in the  $32 h^{-1}$  Mpc simulation; it extends the power law to scales about half as large, as one would expect from the halving of  $r_{\text{smoo}}$ . The results are promising, but the choices of  $r_{\text{smoo}}$  for DENMAX and DENMAX<sup>2</sup> are still a bit arbitrary, indicating the desirability of a HFA without such free parameters.

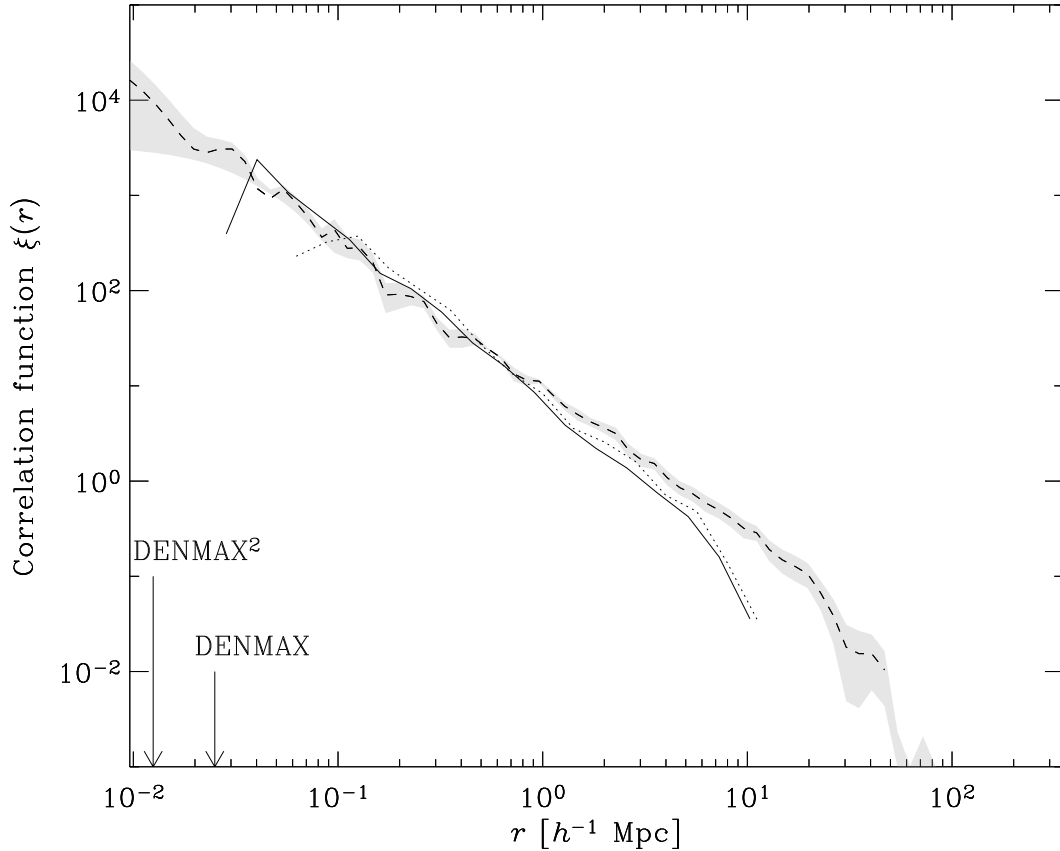


Fig. 4.— The effect of added DENMAX<sup>2</sup> haloes on the correlation function in the 32  $h^{-1}$  Mpc simulation. The dashed curve is the PSCz correlation function, and the grey band shows its errors. The dotted curve is the best fit using just DENMAX haloes, and the solid curve is the best fit including DENMAX<sup>2</sup> haloes. The best-fit central density cutoff was different in each case: for DENMAX,  $\rho_{c,min}$  was 225 particles; for DENMAX<sup>2</sup>, it was 122 particles. The arrows show the DENMAX and DENMAX<sup>2</sup> smoothing lengths: 0.025 and 0.0125  $h^{-1}$  Mpc, respectively.

From the list of DENMAX and DENMAX<sup>2</sup> haloes, we had to pick a subset which we thought could represent PSCz galaxies. Since DENMAX returns the mass of each halo, this was an obvious property to use to characterize haloes. However, DENMAX<sup>2</sup>, with its smaller  $r_{\text{smoo}}$ , systematically returns a smaller mass than DENMAX for the same halo, and we wanted to apply the same criterion to DENMAX and DENMAX<sup>2</sup> haloes. Figure 5 shows that the central density of a halo, estimated by counting the number of particles within a fixed radius  $r_\rho$  of the halo’s center of mass as returned by DENMAX, is well-correlated to its DENMAX mass. For the  $32 h^{-1}$  Mpc simulation, we used  $r_\rho = 20 h^{-1}$  kpc. At twice the softening length, this was about the smallest scale at which we could expect to obtain a meaningful density estimate. Unfortunately, we could not use the same  $r_\rho$  for the larger simulations, because the mass resolution became too poor, causing the density estimate within a small region to be dominated by Poisson noise. So, we simply increased  $r_\rho$  in proportion to the box size of the simulation.

We then had two numbers characterizing each halo: the central density  $\rho_c$  and a mass returned by either DENMAX or DENMAX<sup>2</sup>. To compare haloes from DENMAX and DENMAX<sup>2</sup>, we could either use central density by itself, or try to “correct” DENMAX<sup>2</sup> masses to DENMAX levels. DENMAX<sup>2</sup> masses could be corrected either by knowing how both DENMAX and DENMAX<sup>2</sup> mass scale with central density, or by comparing the DENMAX masses of each halo split by DENMAX<sup>2</sup> to the DENMAX<sup>2</sup> mass of its largest subhalo. We chose to characterize them only by central density, since we felt this was both simpler and more consistent.

We then picked subsets of the halo list according to a lower density cutoff  $\rho_{c,min}$ ; it is physically reasonable that the central density in a halo must exceed some threshold to house an observed galaxy. We first imposed the density cutoff on the list of DENMAX haloes. If reapplication of DENMAX split a halo in the resulting subset into subhaloes, we imposed the density cutoff on each of the subhaloes. If none of these subhaloes exceeded the density cutoff, the original halo stayed in the list; otherwise, any dense-enough subhaloes replaced the original halo in the list.

We then calculated the haloes’ power spectrum by binning halo pairs by their separation, and then submitting the resulting correlation function to an FFT (actually FFTLog, Hamilton 2000). We also tried two other methods. In the first, we calculated the density on a mesh, using the Nearest Grid Point interpolation scheme, and found the power spectrum using a 3D FFT. To get to the smallest scales, Klypin (private communication, 2001) pointed out that if one divides a box of particles into octants (or some other number of equal parts), and overlays all of the octants on each other, periodic boundary conditions will still be satisfied, and the power spectrum of the condensed box should be the same as that of the

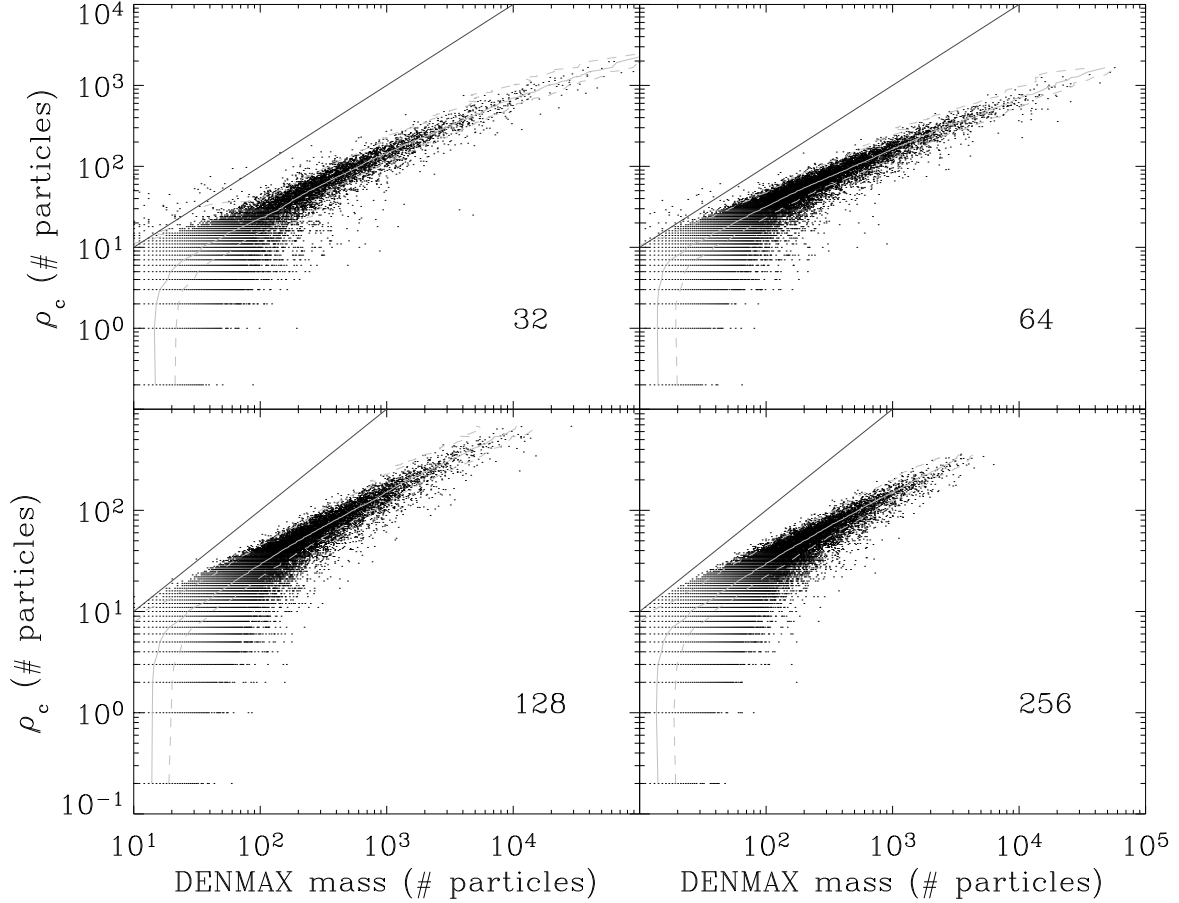


Fig. 5.— Scatter plots of DENMAX mass (number of particles in the halo) versus central density  $\rho_c$  (the number of particles within radius  $r_\rho$ ) for all simulations. Haloes with  $\rho_c = 0$  are shown with  $\rho_c = 0.2$ . No haloes had a DENMAX mass under 10 because DENMAX discards haloes with less than 10 particles. For each  $\rho_c$  which occurred in the distribution, we calculated the average and standard deviation of masses of haloes with  $\rho_c$  within 1/10 of a dex. The solid grey lines show the average mass, and the dashed grey lines are one standard deviation away from the mean. The thin, dashed black line shows the identity function,  $y = x$ , which would result if all, and only, particles counted in the DENMAX mass were within  $r_\rho$  of the halo center.

larger box. This approach did work rather well, but there were small discrepancies between power spectra from different octant overlayings, and it was not obvious how to combine them. Another method we tried used an unequally-spaced FFT (Beylkin 1995), which uses multiresolution analysis (wavelets) to calculate the exact FFT of a set of delta functions in mass (i.e. particles), but a sufficiently large unequally-spaced FFT required more memory than was convenient. These other methods agreed well with the correlation function technique, but we ended up using the correlation function technique because it is possible to calculate the exact correlation function of a relatively small number of haloes quickly with no resolution limit. Also, this technique is not subject to the vagaries of window functions which exist for standard FFTs.

While it is more direct to calculate a correlation function than a power spectrum from a simulation, the opposite is true for a redshift survey such as PSCz. This is because the power spectrum in directions transverse to the line of sight in a redshift survey is unaffected by redshift distortions, which is not true for the correlation function. So, in comparing simulations to observations, it was always necessary to translate one set of data into the same space (either real or Fourier) as the other. Empirically, the correlation function varied more dramatically on the small-scale end with the density cutoff  $\rho_{c,min}$ , and also it is easier to interpret directly in terms of physical pairs of haloes, so we used the correlation function for fitting. It would have been better in principle to use the errors in the power spectrum, since they are more directly measured from PSCz. However, HT have not at present found a positive-definite covariance matrix for the PSCz power spectrum. Thus any comparison we make to simulations would not be completely rigorous anyway. We were still able to estimate the goodness of fit by ignoring cross-correlations among data points (just using HT’s error bars), making a “pseudo- $\chi^2$ ” ( $\tilde{\chi}^2$ ) statistic. Where  $\xi$  denotes the correlation function, and  $b$  is the box size of a simulation, we included  $\xi(r)$ ’s with  $r$  between  $b/256$  and  $b/2$ ; with our bins  $r_i$  varying as they did by a factor of  $\sqrt{2}$ , this included 14 points in the fit. We calculated  $\tilde{\chi}^2 = \sum_i \left( \frac{\xi(r_i) - \xi_{\text{PSCz}}(r_i)}{\sigma_{\text{PSCz}}(r_i)} \right)^2$ , where  $\xi_{\text{PSCz}}(r)$  is the PSCz correlation function at  $r$ , and  $\sigma_{\text{PSCz}}(r)$  is the error in  $\xi_{\text{PSCz}}(r) = \left| \frac{\xi_+ - \xi_-}{2} \right|$ , the average of the upper and lower error bars as reported by HT.  $\xi_{\text{PSCz}}$ ,  $\xi_-$ , and  $\xi_+$  were logarithmically (or linearly, if adjacent data points straddled zero) interpolated if necessary.

### 3. Results

Figure 6 shows the best individually-fit power spectra from each simulation, and the associated  $\tilde{\chi}^2$  curves appear in Fig. 8. Fig. 9 shows the  $\tilde{\chi}^2$  curves as a function of halo number density. Figures 7 and 10 show an alternative collective fit, still varying a central

density cutoff, but constraining the halo number density to be the same in the smallest three simulations; see §3.1.1 for further discussion. With the first of these fits, we have reproduced the form of the PSCz power spectrum on scales  $k \lesssim 40 h \text{ Mpc}^{-1}$ , or  $r \gtrsim 0.05h^{-1} \text{ Mpc}$ . The softening length was  $0.01h^{-1} \text{ Mpc}$ , so this is not much worse than one would hope for given that haloes are many-particle, extended objects which necessarily exclude each other on scales comparable to their radius. Correlation functions and power spectra appear with their theoretical error bars in Figs. 11 and 12. The correlation functions turn down at large scales because waves start to damp out as one approaches half the box size. These figures also show the dark matter correlation functions from each simulation; see Fig. 2 for a clearer view of their relationships. The error bars in the correlation function were calculated by splitting the simulation volume into octants and calculating correlation functions in each. The error at  $\xi(k)$  is then  $\sqrt{[\text{Var}(\xi_i(k))]/8}$ , where  $i$  runs over all octants. The same technique was used to calculate power spectrum error bars.

Figure 1 shows the dark matter power spectra along with a nonlinear power spectrum predicted using the formalism of Peacock & Dodds (1996). The simulated spectra are close to the prediction, although systematically a bit lower. This is not problematic, necessarily, since the Peacock & Dodds method is not exact. Fig. 2 shows a plot of the bias factor  $b(k) = \sqrt{P_{\text{haloes}}(k)/P_{\text{dm}}(k)}$ , a measure of the difference between the galaxy and dark matter power spectra, for the four simulations. The small-scale downturns are caused by the halo-finding resolution in each spectrum. The shape of the bias function is similar to what Kravtsov & Klypin (1999) found; the dependence of bias on scale must be similar to this to achieve a power-law form in the galaxy power spectrum, given the inflection in the dark matter power spectrum caused by the onset of nonlinearity, and the turnover back at smaller scales due to virialization.

Table 2 shows the central density cutoffs along with the halo masses (from Fig. 5) they represent, and the number densities of haloes for which  $\rho_{c,min}$  exceeds the cutoffs. We show errors from the mass-to-central-density relationship, but missing are errors arising from the goodness-of-fit, which we did not include since our  $\tilde{\chi}^2$  estimate is not rigorous. These errors could be sizable, though, particularly in the  $256 h^{-1} \text{ Mpc}$  simulation. The minimum at 6 particles in Fig. 8 for the  $256 h^{-1} \text{ Mpc}$  simulation’s haloes is quite shallow. The  $\tilde{\chi}^2$  value including all detected haloes ( $\rho_{c,min} = 0$ ) was only slightly greater than at  $\rho_{c,min} = 6$ . Using either cutoff, most of the haloes are right at the detection limit (a DENMAX mass of 10 particles), so it is quite possible that the mass resolution in this simulation is insufficient to pick up the true best-fit population of haloes.

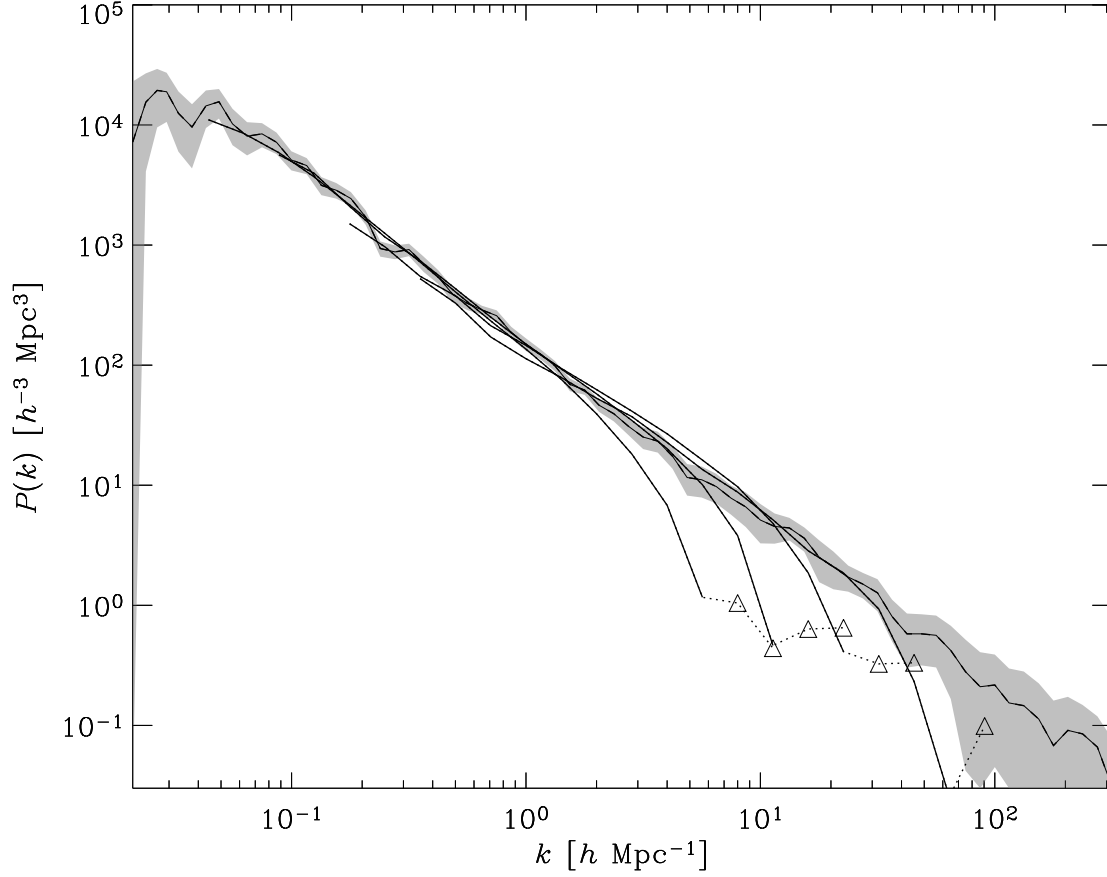


Fig. 6.— The best-fit power spectra (see Fig. 11 for error bars) for all simulations. The PSCz power spectrum is the dotted curve with a grey error band; the best fits from the (from left to right) 256, 128, 64, and 32  $h^{-1}$  Mpc simulations appear as solid curves. Triangles connected with dotted lines denote negative values.

Table 2: Fit Information.

Box size $b$ [ $h^{-1}$ Mpc]	32	64	128	256
$\rho_{c,min}$ [# particles]	122	66	22	6
Halo mass $m_b$ [# particles]	$764 \pm 322$	$269 \pm 121$	$71 \pm 31$	$17 \pm 8$
Halo mass ratio $m_b/m_{2b}$	$2.8 \pm 1.8$	$3.8 \pm 2.4$	$4.2 \pm 2.7$	
Physical halo mass [ $10^{11} h^{-1} M_{\odot}$ ]	$1.4 \pm 0.6$ ,	$4.0 \pm 1.8$	$8.4 \pm 3.7$	$16 \pm 8$
Halo number density [ $h^3 \text{ Mpc}^{-3}$ ]	0.0244	0.0175	0.00873	0.0061

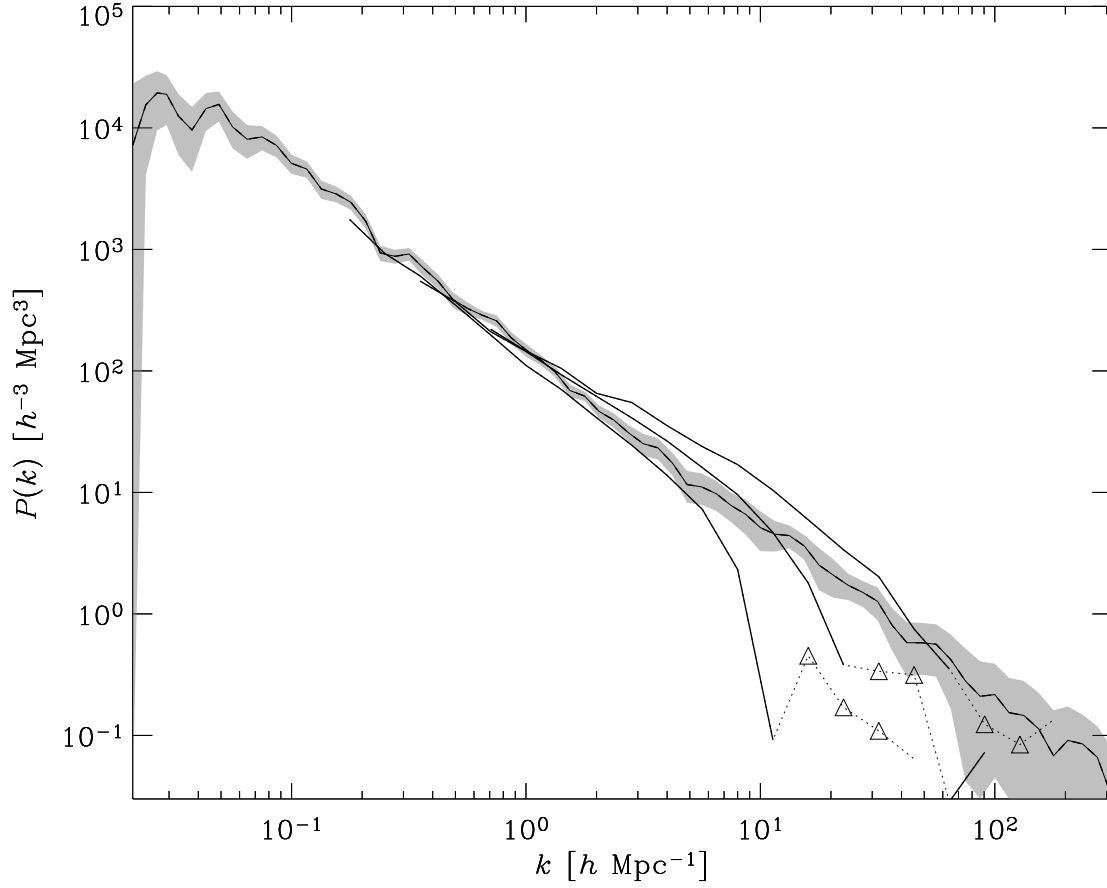


Fig. 7.— The best-fit power spectra (error bars are similar to those in Fig. 11) for the 128, 64, and  $32 h^{-1} \text{Mpc}$  simulations, constrained so that the halo number density matches. Triangles connected with dotted lines denote negative values.

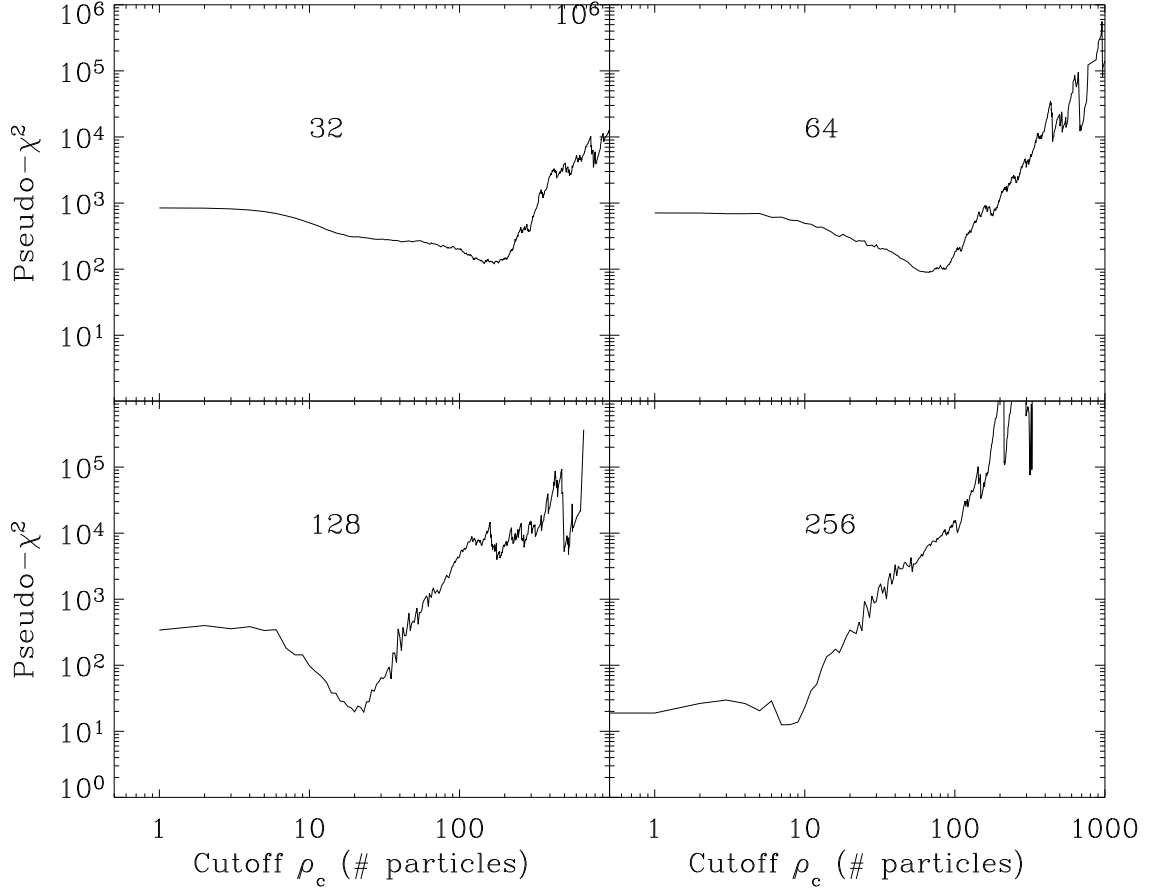


Fig. 8.—  $\tilde{\chi}^2$  values for the four simulations as functions of central density cutoff  $\rho_{c,min}$ . In the  $256 h^{-1} \text{ Mpc}$  simulation, the  $\tilde{\chi}^2$  value at  $\rho_{c,min} = 0$  (including all detected haloes) is shifted to  $\rho_{c,min} = 0.5$  so that it can appear on a log-log plot.

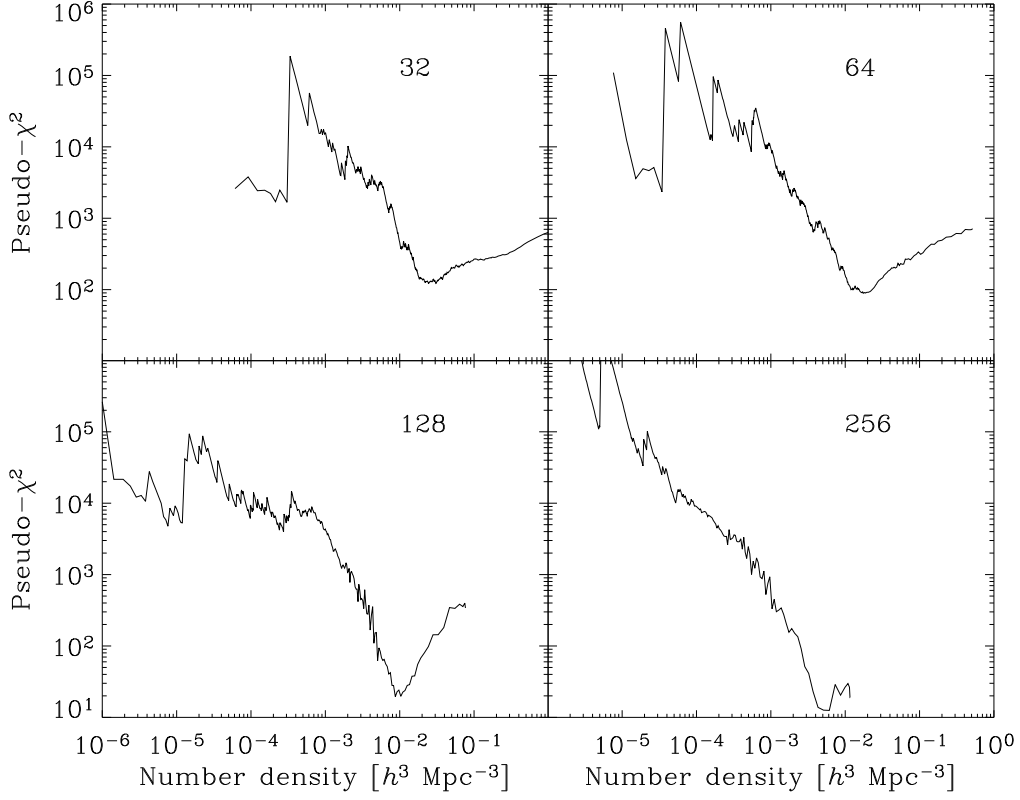


Fig. 9.—  $\tilde{\chi}^2$  values for the four simulations as functions of halo number density. The best-fit number densities are 0.0244, 0.0175, 0.00873, and 0.00611 haloes per  $h^{-3} \text{ Mpc}^3$  for the 32, 64, 128, and 256  $h^{-1} \text{ Mpc}$  simulations, respectively.

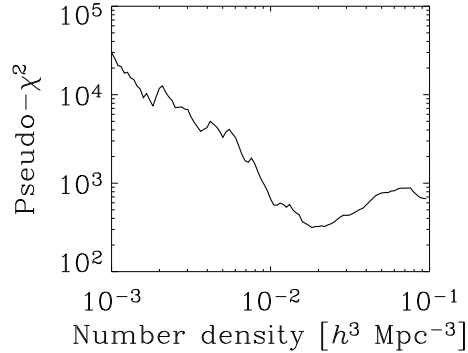


Fig. 10.— The sum over the smallest three simulations of  $\tilde{\chi}^2$  as a function of halo number density. The best fit is at 0.0182 haloes per  $h^{-3} \text{ Mpc}^3$ , which corresponds to the PSCz galaxy number density at a depth of about 20  $h^{-1} \text{ Mpc}$ .

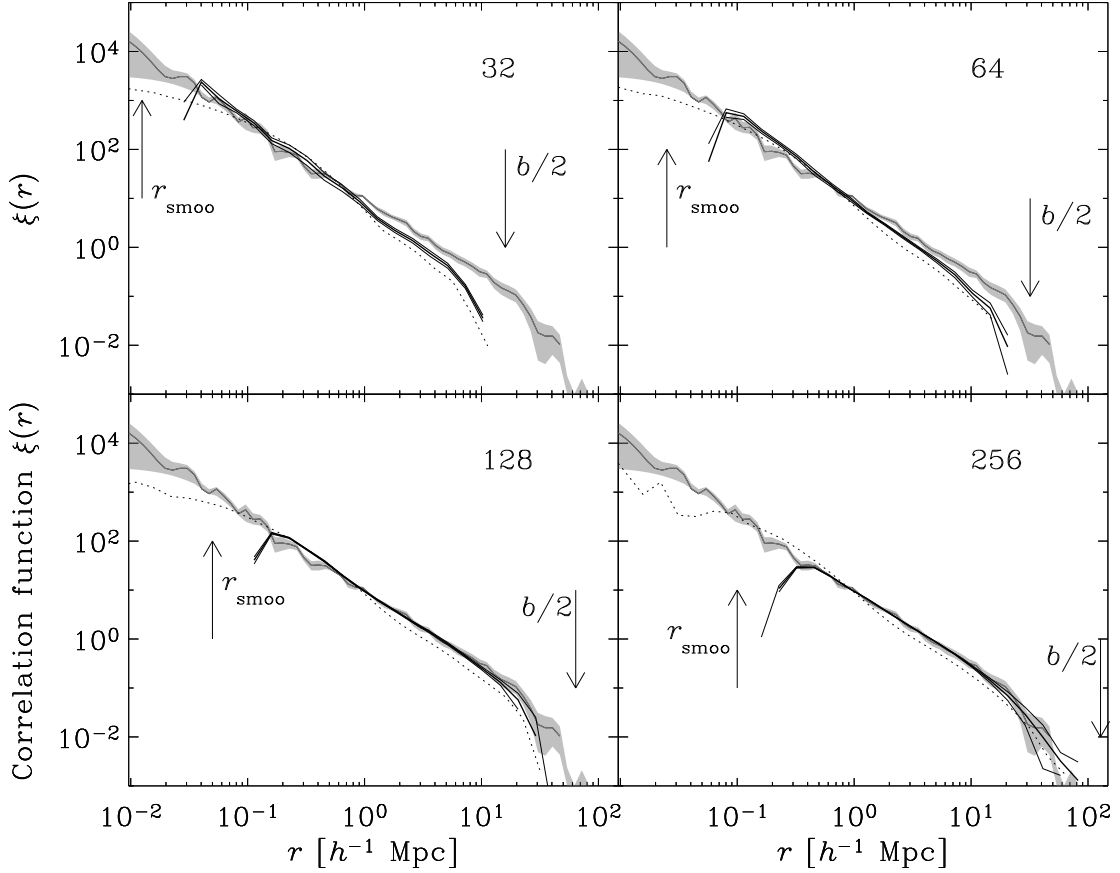


Fig. 11.— The best-fit halo correlation functions (thick solid curves) shown individually with error bands (thin solid curves). The PSCz correlation function appears as a light curve with grey error bands, and the simulations’ dark matter correlation functions appear as dotted curves. Arrows show the scales of the DENMAX<sup>2</sup> smoothing length  $r_{\text{smoo}}$  ( $b/2560$ ), and half the box size ( $b/2$ ), where the correlation function in a box of size  $b$  becomes meaningless. All softening lengths were  $0.01 h^{-1}$  Mpc.

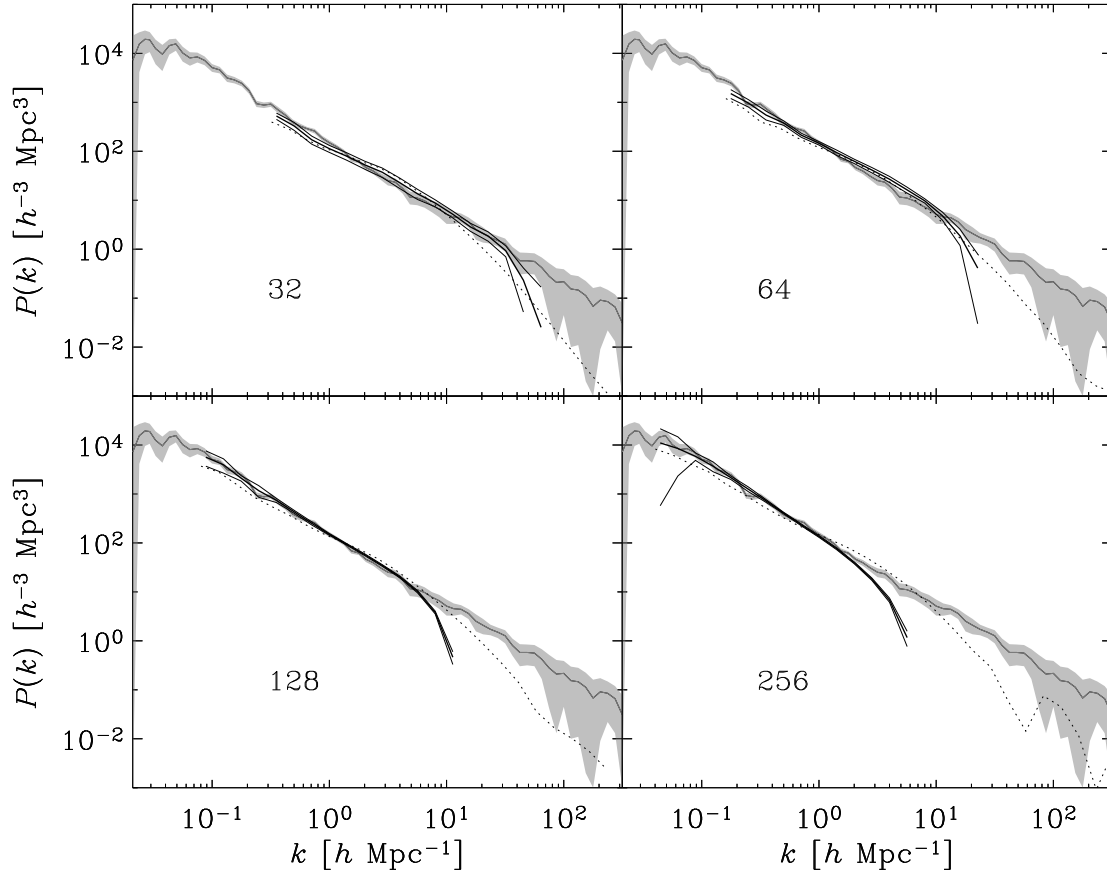


Fig. 12.— The best-fit halo power spectra (thick solid curves) shown individually with error bands (thin solid curves). The PSCz power spectrum appears as a light curve with grey error bands, and the simulations’ dark matter power spectrum appear as dotted curves.

### 3.1. Discussion

Figure 6 shows good fits to the PSCz power spectrum for each simulation, but the question remains: could these haloes from four different simulations represent the same set of haloes? We do not expect them to be exactly the same populations, since in a smaller box, the higher mass and DENMAX<sup>2</sup> spatial resolutions produce more haloes with small separations, many of which could join together in a lower-resolution simulation; this fact is evident in the increased small-scale range of the correlation functions in each simulation. However, there are two apparent discrepancies which must be understood in Table 2: in halo number density and in implied mass cutoff.

One possible explanation for the different-looking halo populations is cosmic variance; i.e. that our chosen set of initial conditions was funny in some way. For example, because of periodic boundary conditions, the  $32 h^{-1}$  Mpc simulation is not big enough to contain the local supercluster from the PSCz cube we used to pick the initial conditions. We measured the correlation functions of haloes in the central  $16 h^{-1}$  Mpc cube of each simulation, first applying the shifts and deformation tensors necessary to put the larger simulations on top of the  $32 h^{-1}$  Mpc simulation. Figure 13 shows the results of this test, for both the individually-fit and number density-constrained central density cutoffs. The central box is evidently undercorrelated relative to the larger boxes, but the correlation functions from different simulations seem consistent with each other, even when the sets of haloes are constrained to have the same number density.

To try to understand the behavior of DENMAX mass and halo number density across the simulations, we identified a few haloes by eye in the central regions of the four simulations. We looked for large haloes near each other across the simulations, and then visualized them with the `points` program written by Michael Blanton, at <http://physics.nyu.edu/~mb144/graphics.html>. Identifying the same halo in each simulation was complicated by the bulk motion and distortion of the central regions, as discussed at the end of §2.1. We found four obvious haloes; the numbers of particles which comprised them in the  $256 h^{-1}$  Mpc simulation were 636, 501, 100, and 89. Fig. 14 shows the 100-particle halo in each simulation, and Fig. 15 shows density profiles for the four haloes identified across the simulations. In the next two sections, we will discuss what we learned from these haloes.

#### 3.1.1. Number Density

From Table 2, the number density of best-fit haloes changes by a factor approaching two between adjacent simulations. To gauge the severity of this potential problem, we

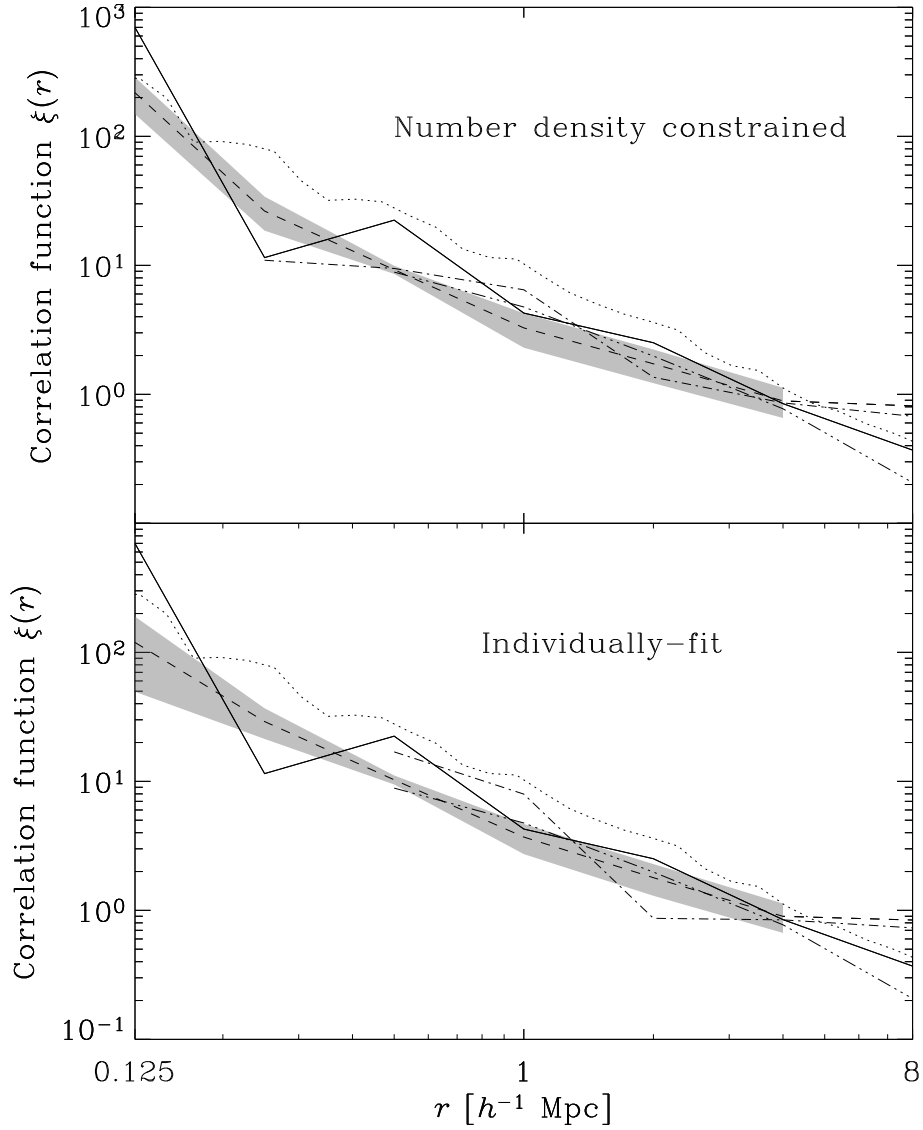


Fig. 13.— Best-fit halo correlation functions measured from the central cube of length  $16 h^{-1}$  Mpc from each simulation, when constrained to have matching number densities and when individually fit. The larger halo sets have been mapped using the shift and deformation described at the end of §2.1 onto the  $32 h^{-1}$  Mpc central region before finding the correlation function. To boost the number of pairs, we actually calculated the cross-correlation of haloes in the central boxes with all haloes in the box in each case. The PSCz correlation function is the dotted curve, and correlation functions from the  $32$ ,  $64$ ,  $128$ , and  $256 h^{-1}$  Mpc simulations appear as solid, dashed, dashdotted, and dashdotdotted curves, respectively. We have put error bands (measured as previously by dividing the region into octants) around the  $64 h^{-1}$  Mpc correlation function, which are typical of the others.

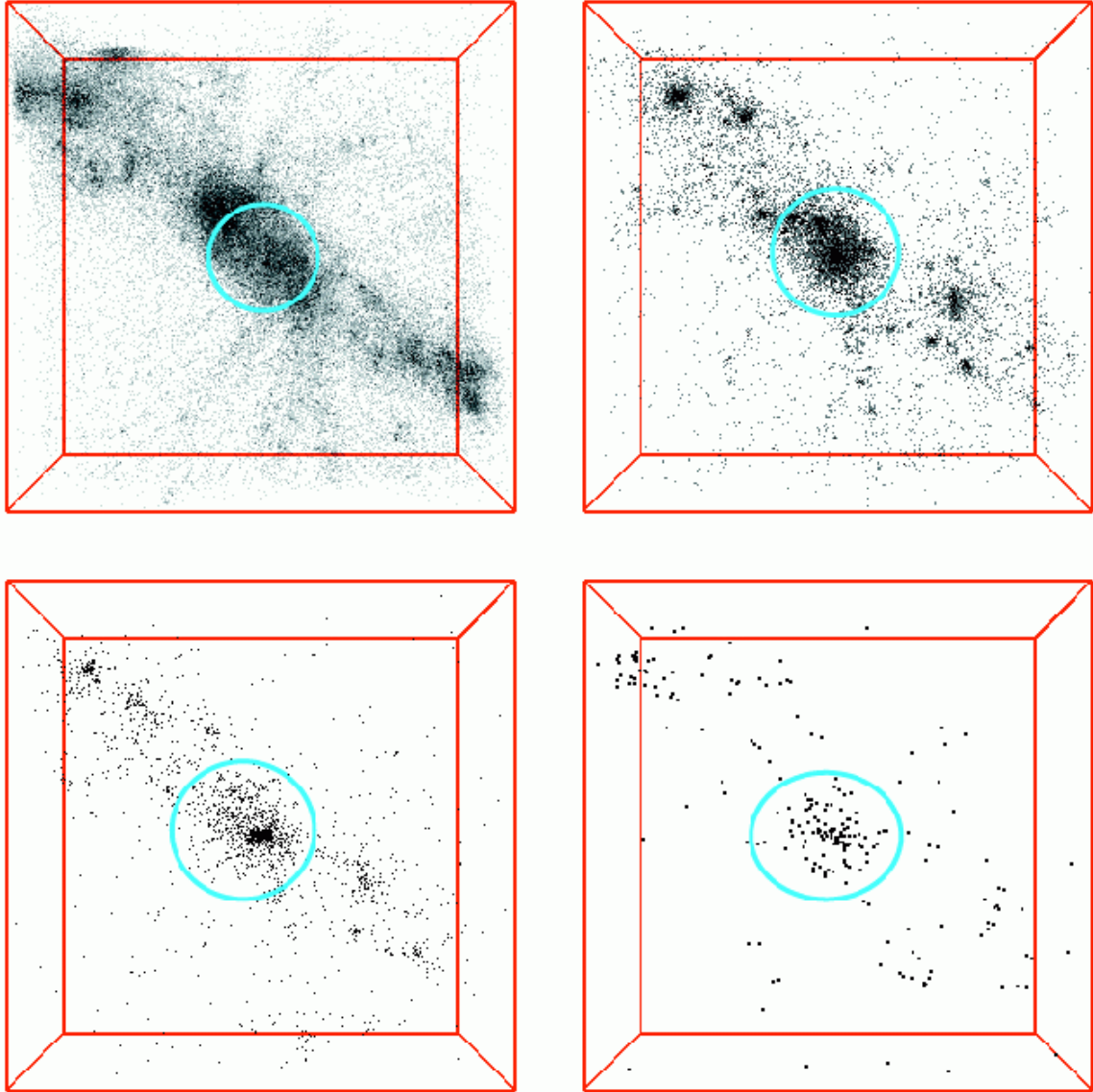


Fig. 14.— The twenty-sixth-largest halo in the  $32 h^{-1}$  Mpc simulation, with a mass of a few times  $10^{12} M_{\odot}$ , in cubes  $4 h^{-1}$  Mpc on a side from each simulation. All particles are shown, but their sizes or opacities vary with mass resolution. Minimally-sized enclosing ellipses are drawn around the actual haloes.

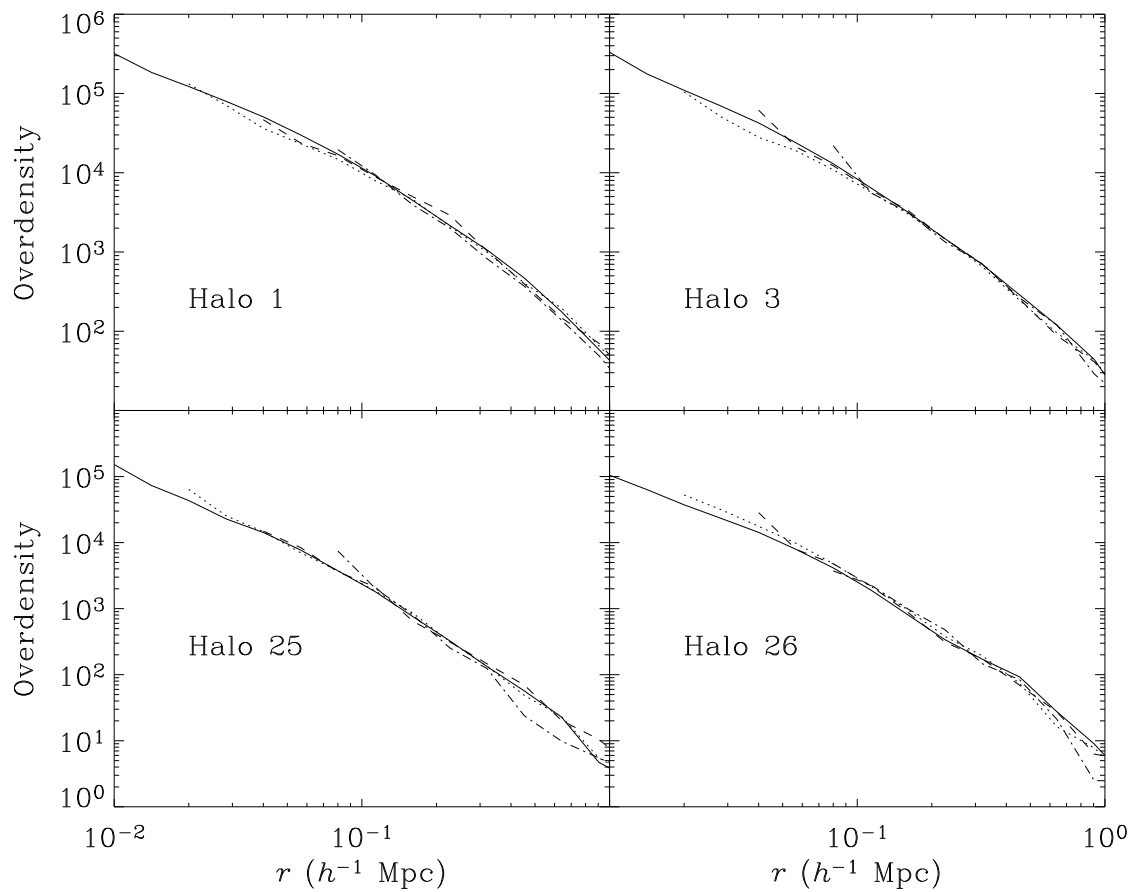


Fig. 15.— Density profiles, as a function of distance from their DENMAX centers, of the four haloes identified across the simulations. The solid, dotted, dashed, and dashdot curves are from the 32, 64, 128, and 256  $h^{-1}$  Mpc simulations, respectively. The halo appearing in Fig. 14 is in the bottom-right corner.

investigated the effect of forcing the number density of haloes in each box to match. Figure 9 shows  $\tilde{\chi}^2$  as a function of halo number density. Excluding the  $256 h^{-1}$  Mpc simulation because it was not clear that the desired set of haloes was well-resolved, and adding together  $\tilde{\chi}^2$  values from other simulations with equal weight, we obtained a total  $\tilde{\chi}^2$  curve, which appears in Fig. 10. The best-fit number density from Fig. 10 was  $0.0182 h^{-3} \text{ Mpc}^3$ , which matches the number density of PSCz galaxies that are about  $20 h^{-1}$  Mpc from the Milky Way. Fig. 7 shows the resulting power spectra, which are not particularly consistent, either with each other or with PSCz. The number density constraint allows smaller haloes into the  $128 h^{-1}$  Mpc set, which lowers the power spectrum; it has the opposite effect on the  $32 h^{-1}$  Mpc set, removing smaller haloes and lifting the power spectrum.

However, it is not obvious that we should expect the same number density of haloes when resolution changes. Suppose we have a set of  $N$  haloes in a box of volume  $V$ . To measure the correlation function, we bin pairs of haloes by distance  $r_i$  to obtain  $P(r_i)$ , the number of pairs in bin  $i$ , with volume  $V(r_i)$ . The value of the correlation function  $\xi(r_i)$  in bin  $i$  is then given by:

$$\xi(r_i) + 1 = \frac{V}{V(r_i)} \frac{P(r_i)}{N^2}. \quad (3)$$

The RHS expresses the number of halo pairs in a bin, normalized by dividing by three quantities: the volume of the bin, the number of haloes, and the mean halo number density. Now suppose that each of these haloes in fact consists of two subhaloes which become resolved when the resolution increases, and that all separations between these subhaloes are much smaller than the  $r_i$ 's. Each pair turns into four, and  $N$  doubles. The new correlation function  $\xi'$  over the previous range of  $r_i$ 's is given by

$$\xi'(r_i) + 1 = \frac{V}{V(r_i)} \frac{4P(r_i)}{(2N)^2} = \xi(r_i) + 1, \quad (4)$$

and pairs also appear in new, smaller-scale bins, imparting to the correlation function there a value possibly as large as the other  $\xi(r_i)$ 's, depending on the bin size and distribution of subhalo distances. So in this simple case, when a higher spatial resolution reveals more substructure, the halo number density increases without changing the correlation function except in new, smaller-scale bins.

Might this model resemble our simulations? Table 3 shows how the number of subhaloes uncovered by DENMAX<sup>2</sup> changes with box size for the four haloes we identified. This table includes all subhaloes, not merely the ones which make the central density cutoff. Also, these are relatively large parent haloes, more likely to have substructure than smaller ones. So although the number of subhaloes generally increases by a factor greater than two as the boxsize halves, the simplistic doubling of haloes in the above model may not be altogether ridiculous.

### 3.1.2. Mass cutoff

Where  $m_b$  is the DENMAX mass (in number of particles) of a halo in a simulation of box size  $b$ ,  $m_b/m_{2b}$  should ideally be 8, the same factor by which the mass resolution changes. The values of  $m_b/m_{2b}$  for the best fits in Table 2 fall well short of this. There are a few possible explanations. Probably, neither central density nor DENMAX mass is by itself a perfect quantifier of how amenable a halo is to galaxy formation. The mean cutoff density  $\rho_c$  versus DENMAX mass relationships in Fig. 5 are monotonic, but it is not true that every set of haloes characterized by a central density cutoff can also be produced with a DENMAX mass cutoff, although the statistical differences may be slight. Also, DENMAX mass is not completely reliable under changes of mass resolution. Even if DENMAX mass were reliable, it would not mean that it is associated simply with a mass which might be observed of a halo in nature. We could have looked at the behavior of  $\rho_c$  in different simulations, but there is not a simple ideal relationship that  $\rho_c$  should satisfy, because the mass resolution, the spatial resolution, and  $r_\rho$  all change differently across the simulations.

We found that, for our four-halo sample,  $m_{32}/m_{64} = 6.3 \pm 0.8$ ,  $m_{64}/m_{128} = 6.1 \pm 0.6$ , and  $m_{256}/m_{128} = 7.3 \pm 0.5$ , somewhere between the ratios in Table 2 and the expected value of 8. This small sample, which includes the largest and third-largest haloes in the  $32 h^{-1}$  Mpc simulation, is statistically biased to large, isolated haloes, which are most likely to be identical across simulations. This probably inflates the mass ratio estimates, since structures are more likely to divide into separate, smaller haloes when the mass resolution is increased. So, the systematic shrinkage of DENMAX mass with increased resolution can partially account for the mass disparity in Table 2. Also, Fig. 14 shows a shrinkage in the physical size of a halo with mass resolution, which corroborates this effect.

Table 3: Splitting of the same haloes with decreasing box size (and thus decreasing DENMAX<sup>2</sup> smoothing length). The halo number is the mass rank in the  $32 h^{-1}$  Mpc simulation DENMAX list, and  $b$  denotes the box size, in  $h^{-1}$  Mpc.

$b$	Halo 1	Halo 3	Halo 25	Halo 26
32	55	55	29	25
64	19	20	9	10
128	4	3	6	3
256	2	1	1	1

## 4. Conclusions

We have shown that we can reproduce the clustering properties of infrared-selected PSCz galaxies fairly well in simulations for scales  $k \lesssim 40 h \text{ Mpc}^{-1}$ , near our resolution limit, by imposing a central density cutoff on haloes. This central density cutoff implies a rough dark matter mass cutoff in PSCz galaxies of  $10^{11-12} M_{\odot}$ . Thus, it appears that dark matter physics alone is sufficient to describe the distribution of PSCz galaxies on the scales we probed. It is doubtful that a simple central density cutoff exists for haloes which house PSCz galaxies in nature, but it seems that central density is still a decent indicator of the hospitality of haloes toward nascent galaxies. While the fits look good, their full statistical assessment awaits a covariance matrix for the PSCz power spectrum.

We have also found that the best-fit halo populations from the four simulations are probably consistent with each other. Their number densities and mass cutoffs do increase systematically with spatial resolution, but we do not believe that these discrepancies indicate that the populations are necessarily inconsistent. One might in fact expect the halo number density to increase when higher resolution reveals more substructure, without affecting the correlation function. Also, the varying mass cutoff is at least partially an artifact of our halo-finding algorithm. We are currently considering new methods to identify haloes with fewer free parameters, which we hope will coax the tips even more confidently from their simulated dark matter icebergs.

## 5. Acknowledgments

This work was supported by NASA ATP grant NAG5-10763.

## REFERENCES

- Baugh, C. 1996, MNRAS, 280, 267
- Berlind, A.A., Weinberg, D.H., Benson, A.J., Baugh, C.M., Cole, S., Davé, R., Frenk, C.S., Jenkins, A., Katz, N., & Lacey, C.G. 2002, submitted to ApJ. (astro-ph/0212357)
- Berlind, A.A., & Weinberg, D.H. 2002, ApJ, 575, 587
- Benson, A.J. 2001, MNRAS, 325, 1039
- Benson, A.J., Cole, S., Frenk, C.S., Baugh, C.M., & Lacey, C.G. 2000, MNRAS, 311, 793
- Bertschinger, E. 1991, in *After the First Three Minutes*, ed. S. Holt, V. Trimble, & C. Benett (New York: AIP), 297

- Bertschinger, E. 2001, *ApJS*, 137, 1
- Bertschinger, E., & Gelb, J.M. 1991, *Computers in Physics*, 5, 164
- Beylkin, G. 1995, *Applied and Computational Harmonic Analysis* 2, 363
- Binney, J., & Knebe, A. 2002, *MNRAS*, 333, 378
- Cen, R., & Ostriker, J.P. 2000, *ApJ*, 538, 83
- Cooray, A., & Sheth, R. 2002, *Phys. Rept.* 372, 1
- Davé, R., Hernquist, L., Katz, N., & Weinberg, D. 2000, in A. Mazure, O. Le Fèvre, V. Le Brun, eds, *ASP Conference Series*, Vol. 200, *Clustering at High Redshift*, p. 402
- Eisenstein, D.J., & Hu, W. 1999, *ApJ*, 511, 5
- Eisenstein, D.J., & Hut, P. 1998, *ApJ*, 498, 137
- Gelb, J., & Bertschinger, E. 1994, *ApJ*, 436, 467
- Gunn, J.E., & Gott, J.R. III. 1972, *ApJ*, 539, 39
- Hamilton, A.J.S., 2000. *MNRAS*, 312, 257
- Hamilton, A.J.S., & Tegmark, M. 2002, *MNRAS*, 330, 506
- Katz, N., Hernquist, L., Weinberg, D.H. 1992, *ApJL*, 399, 109
- Kauffmann, G., Colberg, J.M., Diaferio, A., & White, S.D.M. 1999, *MNRAS*, 303, 188
- Kravtsov, A.V., & Klypin, A.A. 1999, *ApJ*, 520, 437
- Lewis, I.J., et al. 2002, *MNRAS*, in press. (astro-ph/0202175)
- Mathis, H., Lemson, G., Springel, V., Kauffmann, G., White, S.D.M., Eldar, A., & Dekel, A. 2002, *MNRAS*, 333, 739
- Moore B., 2001, in Wheeler J. C., Martel H., eds, *Proc. AIP Conf. Vol. 586, Proceedings of the Texas Symposium*. Am. Inst. Phys., New York, p. 73
- Peacock, J.A., & Dodds, S.J. 1996, *MNRAS*, 280, L19
- Pearce, F.R., Jenkins, A., Frenk, C.S., White, S.D.M., Thomas, P.A., Couchman, H.M.P., Peacock, J.A., Efstathiou, G., 2001. *MNRAS*, 326, 649.
- Pen, U.-L. 1997, *ApJ*, 490, L127
- Percival, W.J., et al. 2001, *MNRAS*, 327, 1297
- Press, W.H., & Schechter, P. 1974, *ApJ*, 187, 425
- Saunders, W., et al. 2000, *MNRAS*, 317, 55
- Seljak, U. 2000, *MNRAS*, 318, 203

- Sheth, R.K., & Jain, B. 2002, submitted to MNRAS. (astro-ph/0208353)
- Somerville, R.S., Lemson, G., Sigad, Y., Dekel, A., Kauffmann, G., & White, S.D.M. 2001, MNRAS, 320, 289
- Wang, X., Tegmark, M., & Zaldarriaga, M. 2002, Phys. Rev. D 65, 123001
- White, M., Hernquist, L., & Springel, V. 2001, ApJ, 550, L129
- York, D. G., et al. 2000, AJ, 120, 1579
- Yoshikawa, K., Taruya, A., Jing, Y.P., & Suto, Y. 2001, ApJ, 558, 520
- Zehavi, I., et al. 2002, ApJ, 571, 172